2-1-2013

Compliant Head Probe for Positioning Electroencephalography Electrodes and Near-Infrared Spectroscopy Optodes

Paolo Giacometti
Dartmouth College

Solomon G. Diamond
Dartmouth College

Journal of Biomedical Optics

SPIEDigitalLibrary.org/jbo

Compliant head probe for positioning electroencephalography electrodes and near-infrared spectroscopy optodes

Paolo Giacometti
Solomon G. Diamond

SPIE

Compliant head probe for positioning electroencephalography electrodes and near-infrared spectroscopy optodes

Paolo Giacometti and Solomon G. Diamond
Thayer School of Engineering at Dartmouth, 14 Engineering Drive, Hanover, New Hampshire 03755

Abstract. A noninvasive head probe that combines near-infrared spectroscopy (NIRS) and electroencephalography (EEG) for simultaneous measurement of neural dynamics and hemodynamics in the brain is presented. It is composed of a compliant expandable mechanism that accommodates a wide range of head size variation and an elastomeric web that maintains uniform sensor contact pressure on the scalp as the mechanism expands and contracts. The design is intended to help maximize optical and electrical coupling and to maintain stability during head movement. Positioning electrodes at the inion, nasion, central, and preauricular fiducial locations mechanically shapes the probe to place 64 NIRS optodes and 65 EEG electrodes following the 10–5 scalp coordinates. The placement accuracy, precision, and scalp pressure uniformity of the sensors are evaluated. A root-mean-squared (RMS) positional precision of 0.89 ± 0.23 mm, percent arc subdivision RMS accuracy of $0.19 \pm 0.15\%$, and mean normal force on the scalp of 2.28 ± 0.88 N at 5 mm displacement were found. Geometric measurements indicate that the probe will accommodate the full range of adult head sizes. The placement accuracy, precision, and uniformity of sensor contact pressure of the proposed head probe are important determinants of data quality in noninvasive brain monitoring with simultaneous NIRS-EEG. [DOI: 10.1117/1.JBO.18.2.027005]

Keywords: near-infrared spectroscopy; electroencephalography; head probe; multimodal neuroimaging; noninvasive brain monitoring.

Paper 12715 received Nov. 5, 2012; revised manuscript received Jan. 4, 2013; accepted for publication Jan. 7, 2013; published online Feb. 1, 2013.

1 Introduction

We introduce a novel noninvasive head probe for concurrent measurement of neural dynamics from the electroencephalogram (EEG) and hemodynamics from near-infrared spectroscopy (NIRS) related to human brain function. This tool is designed to support neuroimaging research that aims to advance our understanding of the relationship between neural activity and cerebral hemodynamics. The design challenge involved in developing a noninvasive multimodal head probe can be divided between precisely and accurately locating sensors on the scalp, and providing a method for stabilizing those sensors in the desired locations with optimal connectivity. In this work we focus on evaluating the positional precision and accuracy of a compliant head probe developed for whole-head positioning of EEG electrodes and NIRS optodes. We also study the sensor contact pressure on the scalp from the head probe.

EEG and NIRS are particularly conducive to multimodal studies because they measure different aspects of brain activity and because the optical and electrical systems do not interfere with one another. Simultaneously acquired EEG can account for more of the variation in hemodynamics measured with NIRS than a task paradigm alone.[1] This suggests that the covariance in task related responses in simultaneously acquired EEG and NIRS contain additional information about neurovascular function or brain activity that cannot be observed when using these systems sequentially. It has also been suggested that hemodynamic factors can modify neural activity through the so-called hemo-neural hypothesis.[2] The combination of EEG and NIRS is particularly advantageous for quantitatively studying the neurovascular coupling relationship because they share high temporal sampling rates, which for EEG is on the order of 1000 Hz and for NIRS is on the order of 25 Hz. This enables examination of the relationship between neural dynamics and more subtle features in the hemodynamics compared to simultaneous EEG and functional magnetic resonance imaging (fMRI), where the hemodynamic sampling rate is in the order of 0.5 Hz. Combining EEG and NIRS is a potentially cost-effective and easy-to-use way of studying the brain because the instrumentation and personnel requirements are modest compared to fMRI and positron emission tomography (PET). Combined EEG-NIRS has been applied to studies of vision,[3] epilepsy in children,[4–6] and carotid endarterectomy,[7] and in combination with transcranial magnetic stimulation.[8]

1.1 *Multimodal Neuroimaging to Study Neurovascular Coupling*

Research on multimodal neuroimaging including combined EEG-fMRI,[9] magnetoencephalography (MEG) with NIRS,[10] and EEG-NIRS has been suggested as a means to advance the study of human brain function.[11] Measurements of functional brain activation can be obtained in the form of electrical neural activity, metabolic activity, and localized increase of blood volume and oxygenation.[12] Obtaining simultaneous measurements of these signals provides more information about the

Address all correspondence to: Paolo Giacometti, Thayer School of Engineering at Dartmouth, 14 Engineering Drive, Hanover, New Hampshire 03755. Tel: +603-785-2111; Fax: 603-646-0151; E-mail: Paolo.Giacometti@Dartmouth.edu

0091-3286/2013/$25.00

activation[13] and also about the relationship between these signals.[10,14,15] Studying brain function with multiple neuroimaging modalities that combine neural and hemodynamic measurements permits examination of the neurovascular coupling relationship. The neurovascular unit, which includes neurons, capillaries, astrocytes, and micro glia, works as a complex system in order to maintain homeostasis.[16] Dysfunction of the neurovascular unit has been suggested as a causative factor in neurodegenerative disorders such as Alzheimer's disease[16–18] and has also been observed in hypertension and ischemic stroke.[19,20] Studying neurovascular coupling may aid in the development of drug therapies[21] and diagnostics for these diseases[22] as well as increase our understanding of the functioning of the neurovascular unit.[23]

1.2 *Electroencephalography and Near-Infrared Spectroscopy Systems*

EEG is a technique used to measure electric potentials originating from synchronous neuronal activity in the brain.[24] In the noninvasive approach, electrical terminals (electrodes) are placed on the surface of the scalp and are connected to an amplifier to measure and record the electric potential signals. EEG is commonly used clinically to diagnose and monitor patients with neurological diseases such as epilepsy.[25]

NIRS is a technique used to measure changes in blood volume and blood oxygenation.[26] When used with a high-density 263 optode array over the whole head, it is possible for NIRS to measure hemodynamic activity originating from an average of 37% of the cortical surface on adults.[27] Optical terminals (optodes) are placed on the surface of the scalp in order to illuminate near-infrared light into the tissue and detect diffuse light scattered through the tissues and re-emitted from the surface. The NIRS signal from a source-detector pair arises from changes in oxygenation in the volume region between the source and detector, which includes scalp, skull, pial vasculature, and cortex.[28] In the continuous-wave (CW) approach, using two wavelengths or more, the modified Beer-Lambert law can be used to obtain a measure of changes in oxygenation in the head in the form of changes in concentration of chromophores such as oxygenated and deoxygenated hemoglobin.[29] These chromophores have different levels of attenuation of light in the 600 to 900 nm range. Therefore, changes in chromophore concentration can be calculated from changes in light attenuation. When the source and detector optodes are separated by a few centimeters, the spatial sensitivity of source-detector pairs to tissues in the head includes the outer cortical regions from which NIRS brain activity measurements are made. Localized changes in the concentrations of oxygenated and deoxygenated hemoglobin measured with NIRS have been shown to temporally and spatially correlate with metabolic consumption of oxygen measured with PET and fMRI blood oxygen level dependent (BOLD) measures of brain activity.[30] NIRS signals measuring these variations in hemoglobin concentration have been used as a clinical monitor of brain hypoxia.[31] In the research setting, NIRS is commonly used to measure cerebral hemodynamics.[32]

EEG and NIRS systems are low cost and portable, making them convenient tools for bedside and ambulatory neural and hemodynamic monitoring of the brain. The results obtained from EEG and NIRS systems are strongly influenced by several aspects of system setup. Accurate and precise sensor location is needed for anatomic registration, and electrode and optode coupling with the surface of the scalp is needed for data quality. Also, subject comfort and minimization of motion artifacts are affected by the ergonomics of the method used for sensor placement and fastening to the head, while ease of use is needed to minimize user error and set-up time.

1.2.1 *Sensor location*

The layout of EEG electrodes is based on the International 10–20 and 10–10 positioning systems that use the inion, nasion, and preauricular points as fiducial positions. Arcs that follow the contours of the head are formed from connecting these fiducial points.[33] The arcs are evenly subdivided into 10% or 20% arc lengths. This standardized system helps in the interpretation of data as it provides clinicians with the neuro-anatomical correspondence of measurements on the scalp. Standardized positioning minimizes test-retest and inter-subject variability, which aids in diagnosis of patients without having to digitize and register the electrode positions from every recording session.[34,35]

There is no widely accepted standard in place for NIRS optode positioning on the scalp but there have been attempts at creating one in a similar fashion to the international 10–20 system used in EEG.[36] Many different layouts have been used either focusing on a region of interest or patterning over the whole surface of the scalp.[37,38]

Correct sensor positioning is important in NIRS and EEG for neuro-anatomical correspondence and interpretation of the signal sources in the brain. Precise positioning ensures that the sensor is placed on the same location on a particular head every time it is affixed. Accurate positioning ensures that the sensor is placed on the location where it corresponds with respect to the 10–10 standardized system. Placing electrodes using caps has been shown to cause significant electrode positional error, making them an inappropriate method when accuracy is necessary.[39] In this work we aim to demonstrate that our NIRS-EEG head probe can be used to accurately and precisely place electrodes.

1.2.2 *Sensor coupling with the scalp*

Electrical coupling with the scalp refers to the electrical impedance between the electrode and the scalp. Low electrical impedance is desired for high quality EEG because neural signals are in the order of microvolts.[40,41] Scalp impedance values are normally required to be below 5 kΩ so that the signal can be distinguishable from noise, but some studies have obtained reliable data with up to 40 kΩ impedance measurements.[24,42] To maximize electrical coupling, several methods are used to place electrodes on the head such as individual electrode adhesion to the scalp or by using headbands or caps.[43,44] EEG electrolyte pastes or gels are also used to bridge the connection between the electrode and the scalp in order to decrease impedance. Some studies have shown that using dry electrodes that do not require electrolytes can perform comparably to wet electrodes.[45]

Optical coupling refers to the efficiency of light transmission between the optode and the head. Light can be lost both at the point of delivery on the scalp and at the point of detection. To maximize optical coupling, these losses must be minimized. Allowing air gaps in between the optode and the scalp decreases the amount of light that enters the head.[46] Optical coupling is maximized when optodes are placed normal to the surface of the scalp. Doing so maximizes the contact area of the optode and minimizes gaps of air or obstruction due to hair between the optode and the scalp.

Optodes must be affixed in a repeatable manner to ensure test-retest reliability. Also, constant pressure by the optodes on the scalp is necessary because variation in contact pressure can introduce artifacts in the signal intensity. These artifacts can result from movement of the head, optical fibers, or an unsecured optode. Different methods are used to place optodes on the scalp to maximize optical coupling, such as using headbands that fasten pads of optodes to a particular region on the head[26] or mechanisms to hold optodes in a stable manner against the scalp.[47]

1.2.3 *Ergonomics in sensor placement*

Ergonomics in sensor placement refers to the comfort of the subjects when having sensors on his or her head and minimization of the time and the level of difficulty in affixing the sensors by the experimenter.

1.3 *Design Intent of the NIRS-EEG Head Probe*

The head probe is designed to combine NIRS optodes and EEG electrodes into a single cap with whole-head coverage. This combined optode-electrode approach supports simultaneous measurement of neural electrophysiology and vascular hemodynamics for research and clinical studies of neurovascular coupling. The head probe is designed to expand and contract to fit different head sizes and shapes. To facilitate clinical translation, electrodes are placed using the 10–10 expansion of the standard international 10–20 positioning system,[48] and optodes are placed on a subset of the 10–5 positioning system.[49] The head probe is designed to function with a variety of electrode and optode designs and many EEG and NIRS systems.

The focus of the present study is on evaluating the accuracy and precision of electrode and optode positioning and evaluating the uniformity of contact pressure with the scalp. Positional control and contact pressure are fundamentally important aspects of the head probe function that generalize to data quality of any particular electrodes and optodes that are used in the probe.

2 Methods

The NIRS-EEG head probe contains 65 electrodes and 64 optodes, as shown in Fig. 1. Its design is based on an expandable linkage mechanism [Fig. 1(a)] that follows the primary contours of the scalp. Electrodes [Fig. 1(c)] act as joints so that the linkage mechanism can expand and contract to fit the desired head size while maintaining equidistant electrode spacing. An elastomeric web [Fig. 1(b)] attached to the linkage mechanism expands and contracts uniformly together with the linkage mechanism and supplies the contact pressure. The web holds the optodes [Fig. 1(d)] and some of the electrodes in place on the scalp. Electrodes placed at the inion, nasion, preauricular, and central fiducial positions determine the location of all optodes and electrodes by mechanically following the 10–10 coordinate system. The probe is designed to avoid calculating the location of each electrode or optode and placing them on the head individually. Once the fiducials are identified and the corresponding electrodes placed in those locations, the head probe will ensue correct positioning of the electro-mechanical components.

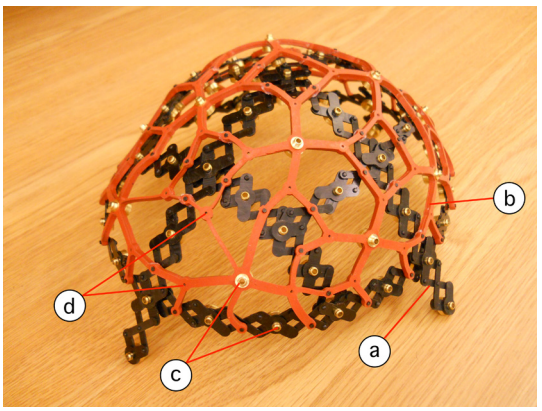

Fig. 1 NIRS-EEG head probe components: (a) linkage mechanism, (b) elastomeric web, (c) electrodes, and (d) optode locations.

2.1 *Probe Design*

The structural elements of the design consist of linkage chains that intersect each other to form a compliant extensible and contractible hemisphere. Electrodes act as joints in the linkage chains to ensure that they remain equidistant while the probe is expanded or contracted. This mechanism is designed to provide accurate standard positioning regardless of head size or shape of the head probe. The web stretches with the expansion of the link mechanism while maintaining contact pressure of the probe on the scalp. The web was designed to provide contact pressure as uniformly as possible over the scalp. The tension in the web holds the head probe in place on the scalp to stabilize the position of the probe. The web holds all the optodes and the electrodes that are not integrated into the linkage mechanism. The electrodes in the prototype shown (Fig. 1) are brass cup electrodes with an injection port for electrode gel. Electrodes and optodes of any kind may be used in the NIRS-EEG probe and are not the focus of this study.

2.1.1 *Web-link element subsystem*

The EEG 10–20 positions are arranged in sagittal and coronal arcs on the scalp.[33] These arcs then cross each other producing a grid over the surface of the head with well-defined regions. For the purposes of probe design, these regions are organizationally very similar to one another, yielding a basic element of linked arms, web, electrodes, and optodes. This element, referred to as a web-link element subsystem (Fig. 2), was used to tile a repeated element design over the surface of the head. Basing the design on a unit that is tiled provides tighter control over the mechanical properties of the design, which aid in the overall structure and homogeneity of the mechanism.

Each web-link element subsystem is composed of four linked chains, one web element, four optodes held at the nodes in the web element, and nine electrodes, one of which is held by the web. As the web-link element subsystem expands and contracts, the web element and link chains expand proportionally keeping all nodal positions the same fractional distances from one another. Since this design is replicated across the probe, the mechanics remain the same throughout. This element-based design allows for placement of optodes and electrodes on a range of head sizes and shapes.

2.1.2 *Linkage mechanism*

The dimensions of the links were calculated following head circumference measurements obtained across age and gender.[50,51] The links were designed to minimize the space covered by the

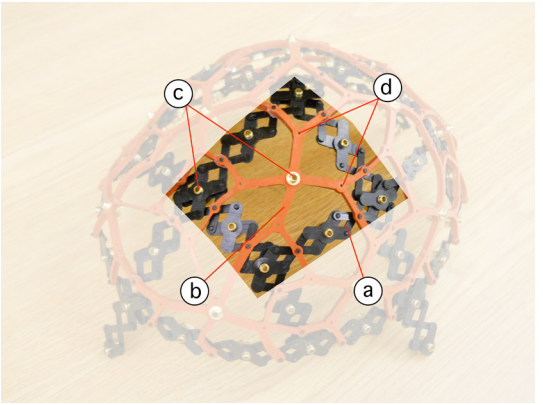

Fig. 2 Web-link element subsystem components: (a) linkage mechanism, (b) elastomeric web, (c) 3 electrodes, and (d) optode locations.

linkage mechanism, and allow for adequate space for electrodes and optodes. The width and thickness of the links were chosen to allow the link chains to be flexible while accommodating the web and electrode integration. The length of the links was chosen to fit normal head size variations using the following geometric calculations.

The minimum and maximum joint-to-joint distance along the link chains determine the size limits of the probe, which determine the head size range that the probe can fit. The maximum joint-to-joint distance can be calculated from geometric relations obtained from Fig. 3. The length of the link (L) can be expressed in terms of measurements of the chain when it is at its maximum extent as

$$L = \sqrt{x_{\max}^2 + y_{\min}^2}, \tag{1}$$

where $x_{\max}$ is the maximum joint-to-joint distance, and $y_{\min}$ is the minimum joint-to-joint height. The angle (θ_1) between the horizontal and the link length at the most extended position of the chain is

$$\sin(\theta_1) = \frac{y_{\min}}{L} = \frac{(w_1 + w_3)/2}{x_{\max}}, \tag{2}$$

where w_1 is the width of the main body of the electrode-link, and w_3 is the width of the joint-link, shown in Fig. 3. Combining Eqs. (1) and (2) and solving for $x_{\max}$ yields

$$x_{\max} = \frac{1}{2}\sqrt{2L^2 + 2L\sqrt{L^2 - w_1^2 - 2w_1w_3 - w_3^2}}. \tag{3}$$

Similarly, the minimum joint-to-joint distance can be calculated from geometric relations obtained from Fig. 4 in the same way as it was done to find $x_{\max}$. The link length L can be expressed as

$$L = \sqrt{x_{\min}^2 + y_{\max}^2}, \tag{4}$$

where $x_{\min}$ is the minimum joint-to-joint distance, and $y_{\max}$ is the maximum joint-to-joint height. The sine of the angle θ_2 between the horizontal and the link length at the chain's most compressed position is

$$\sin(\theta_2) = \frac{y_{\max}}{L} = \frac{(w_2 + w_3)/2}{x_{\min}}, \tag{5}$$

where w_2 is the thickest width of the electrode-link, as shown in Fig. 4. Combining Eqs. (4) and (5) and solving for $x_{\min}$ yields

$$x_{\min} = \frac{1}{2}\sqrt{2L^2 - 2L\sqrt{L^2 - w_2^2 - 2w_2w_3 - w_3^2}}. \tag{6}$$

Since the circumference of the probe is given by the sum of the joint-to-joint distances, the minimum and maximum probe circumference (C) can be obtained as a function of the link design dimensions w_1, w_2, w_3, and L. For the 10–10 EEG positioning system where $C_{\min} = 40x_{\min}$ and $C_{\max} = 40x_{\max}$.

Values for the minimum and maximum inion-nasion (IN) and preauricular (P) arcs can also be obtained noting that $\mathrm{IN} = 20x$ and $P = 20x$. Note also that since the links were designed in two different dimensions d_1 and d_2 for different regions of the linkage mechanism, there are maximum and minimum joint-to joint distances for each region.

2.1.3 *Elastomeric web*

The elastomeric web was designed with variable-thickness segments to maintain uniform contact pressure on the scalp. The web stretches and contracts proportionally preserving the relative position of the sensors. The elastomeric web was designed as a single part, connecting each web element at the joint positions of the link chains. In this way, the web expands and contracts together with the linkage mechanism thus adding tension

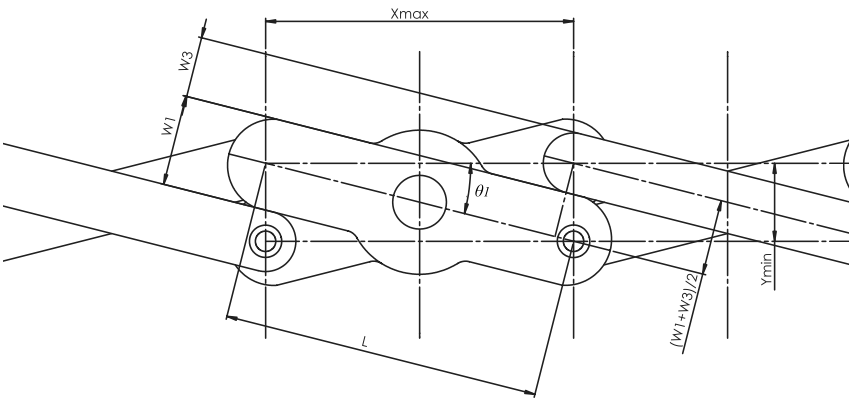

Fig. 3 Link dimensions from an expanded chain.

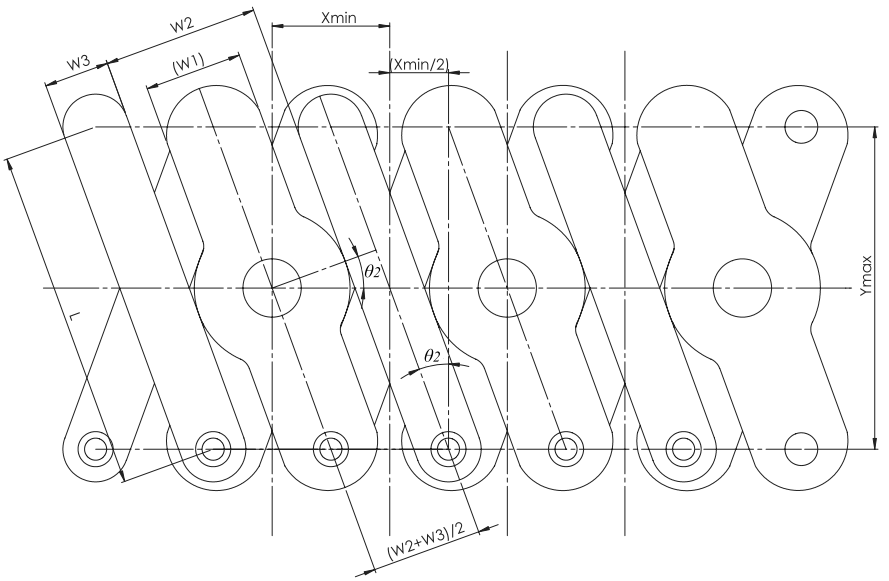

Fig. 4 Link dimensions from a compressed chain.

to the probe and contact pressure on the scalp. Calculations were performed to achieve evenly distributed tension over the elastomeric web. The cross-sectional area of each web segment was sized individually in order to provide uniform elastic force. The web is designed to fit a subset of head sizes to provide a small range of contact pressures. Therefore, several web sizes are needed for a single head probe to accommodate all adult head sizes.

The web design is based upon an MRI-based computer-aided design (CAD) 3-D model of an adult head. This model was produced as an average of a set of mesh-based head models in order to accommodate a range of head sizes.[52] However, this same design process can be performed using a single head model from a particular individual, providing a way to produce webs that are customized. The design process, going from the MRI to the final web was conducted in several steps, as illustrated in Fig. 5.

First, a stack of MRI images obtained from the subject is obtained, and converted into a 3-D volume [Fig. 5(a)]. This volume is then segmented in order to export a volumetric or surface mesh of the head in the form of a stereolitography file [Fig. 5(b)]. This file can be imported into CAD software SolidWorks (SolidWorks Corp., Waltham, Massachusetts) to create a 3-D model of the head [Fig. 5(c)]. Once the model of the head is obtained, 10-10 EEG positions are calculated based on the inion, nasion, and preauricular fiducial positions [Fig. 5(d)].[33,48] Next, a 3-D sketch of the electrode positions is made from the 10-10 EEG positions [Fig. 5(e)]. Based on this sketch, optode locations are calculated following an extension to the 10–10 EEG position system [Fig. 5(f)].

Once the positions of all the optodes and electrodes are known, a 3-D outline of the web is made based on the linkage structure [Fig. 5(g)]. In order to compute the force equilibrium equations for each web element, the web element positions are projected onto a plane. The plane is computed as the one that minimizes the normal projection from all points in the web element. This is done for every web element [Fig. 5(h)]. Once these planes are obtained, a local coordinate system is calculated following the main arcs of the head [Fig. 5(i)]. A series of force equilibrium systems are computed in order to calculate the cross-sectional area of the members in the web elements [Fig. 5(j)]. Even though the planes used for the projection of the coordinates are computed for each web element, the force equilibrium calculations are done independently for each node in the web element. These calculations are carried out so that each node remains stable during expansion and contraction of the web. A program was written in Matlab (The Mathworks Inc., Natick, Massachusetts) to perform the calculations for each node using their own coordinate system.

Once the cross-sectional areas of each arm in the web were obtained, a quadrant of the web was sketched in a plane [Fig. 5(k)]. The widths were calculated by dividing the cross-sectional areas calculated by the thickness of the material being used for manufacturing. The lengths used on the design were 10% smaller than those in the 3-D model in Fig. 5(g) so that when it is placed at the original position it stretches applying a force onto the head. The process of converting a 3-D model to 2-D sacrifices angular accuracy to maintain accurate member lengths and constant forces. The angular approximations are corrected when the web is assembled onto the linkage mechanism. With a known thickness of the material, a model of a quadrant is designed [Fig. 5(l)]. The four quadrants are combined in a single planar design ready for manufacturing [Fig. 5(m)]. The corresponding joints are glued together once the planar web is manufactured in order to convert it again to a 3-D web, as shown on Fig. 6.

2.2 *Sensor Positioning Precision and Accuracy Test*

A test was carried out to validate the sensor placement precision and accuracy provided by the head probe. The test (1) evaluated the accuracy of the positions relative to the standard 10–10 EEG system, (2) examined the repeatability of the position in a test-retest method, and (3) compared the results against a commercial product.

The positions of the electrodes of the NIRS-EEG head probe and the commercial ANT Waveguard (Advanced Neuro Technology, ANT B.V., Enschede, Netherlands) probe were digitized using a 3-D scanner (ExaScan, Creaform Inc., Quebec, Canada) on $N = 10$ subjects. The experimenter affixed the probe and

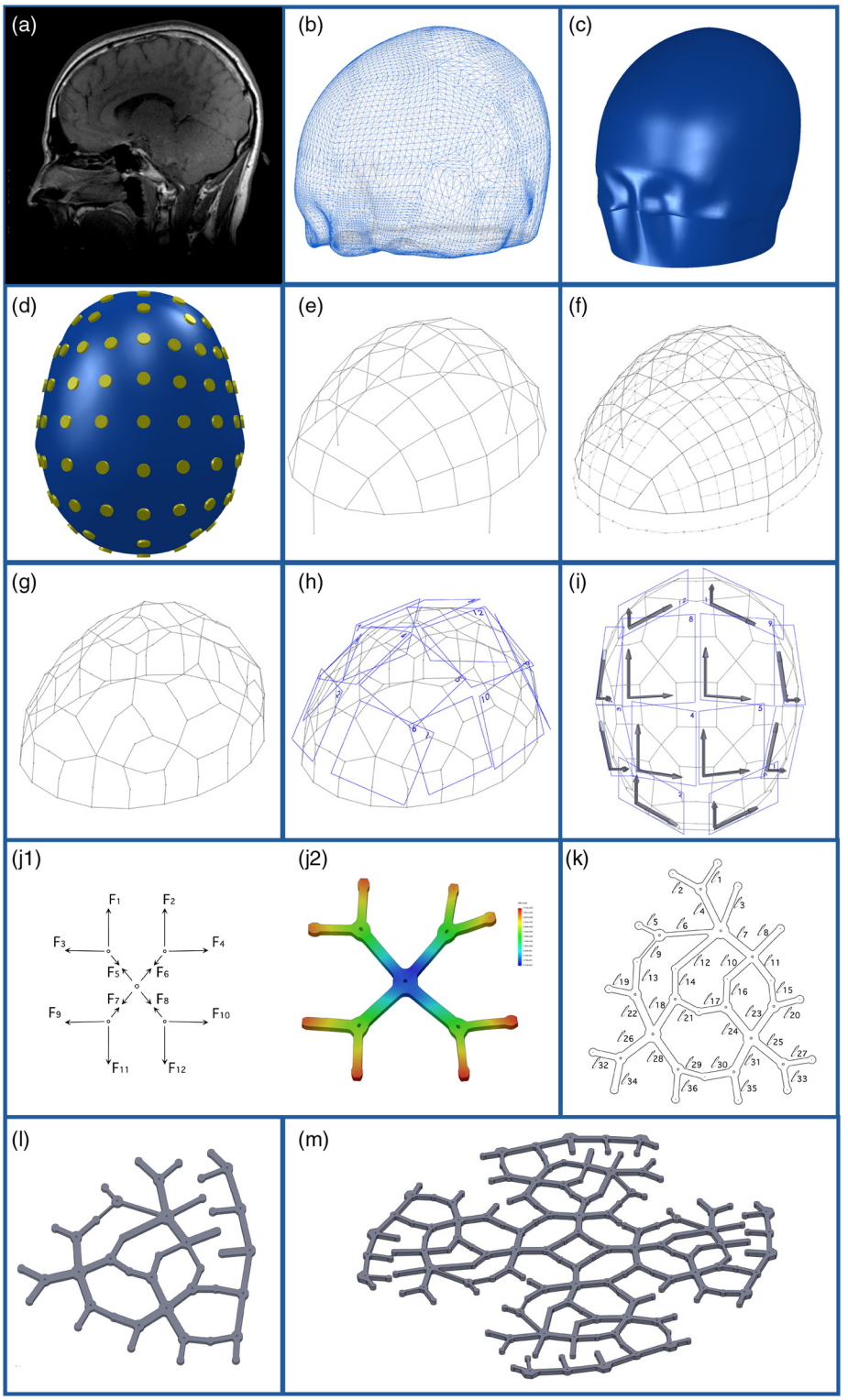

Fig. 5 Web design steps.

scanned the electrode positions three times per subject for each probe, for a total of 30 data sets per probe. EEG 10-10 positions were calculated and carefully placed on a mannequin head in order to have a common reference frame of positions.

The digitized points obtained from the scans were registered within each subject in a two-step process. In the first step, the position sets for each scan were rigidly registered to the scalp positions on the mannequin head by minimizing the sum-squared deviations between all electrodes. This first step enabled the order of the electrode positions to be normalized across all data sets. In the second step, individual within-subject registrations were performed. For this step, the first of the three position data sets was designated as baseline and the second and third position data sets were rigidly registered to the first. The

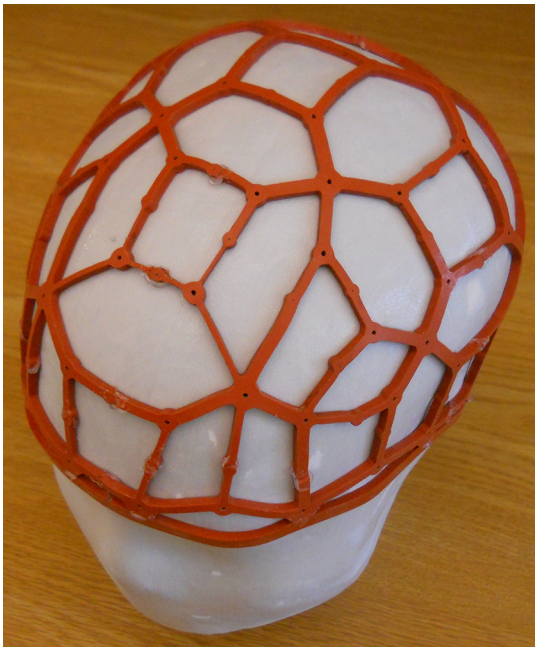

Fig. 6 Elastomeric web.

sum-squared deviations of all electrode positions were again used in the optimization. For the position precision test, the position deviations were computed as the root-mean-squared distances between registered electrode positions and the within subject mean electrode positions.

For the position accuracy test, the arc length accuracy was computed for all the arcs that define the 10–10 positions. Since the 10–10 positions are based on the 10% of each arc length, subdivisions in arc length were computed for all arcs. The distance between positions were then compared to the ideal percent arc length subdivisions of the 10–10 system.

2.3 *Web Volumetric Isotensile Test*

A second test was performed on the elastomeric web in order to evaluate the uniformity of the contact forces of the probe on the scalp.

A Mark 10 BGI force/torque gauge and a SSM2 sensor (both from Mark 10 Corporation, Copiague, New York) were used to measure the force at each web node containing an optode or electrode position (64 optodes and 12 electrodes) as shown on Fig. 7. The head model constructed for the web design

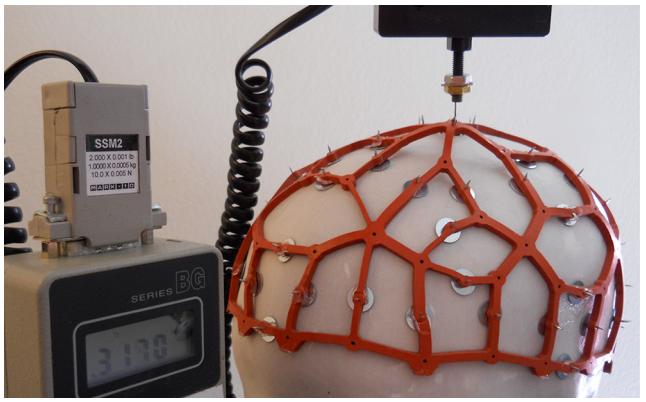

Fig. 7 Volumetric isotensile test setup.

mentioned in Sec. 2.1.3 was 3-D-printed to be used as the test subject. The web was placed on the printed head model. As seen in Fig. 7, the linkage mechanism was not used on this test to isolate the web properties. Tacks glued to the head model were used to support the web as the linkage mechanism would when extended to fit the head model. This method isolated the web during the test. A hook with a planar base was inserted into each node to pull a specific distance normal to the head. The sensor, connected to the hook, was used to pull each node 0.5, 0.75, and 1 cm away from the head model. The force exerted by the members on the node was recorded at each distance. A 100 gram weight was measured between every web force measurement to ensure accuracy.

3 Results

3.1 *Head Probe Design*

The range of sizes that the head probe provides were calculated from the minimum and maximum lengths of the linkage chains in the mechanism. Table 1 shows the sizes for the joint-to-joint distances for the two link dimensions and the main chains using Eqs. (3) and (6).

The values measured for the maximum chain lengths are very similar to the calculated values. As the probe is contracted, the chains interfere with each other and less space is available for them to move any further. This prevents them from contracting to their smallest size, leading to large differences between the calculated and measured lengths. Even though there are differences, the head probe's minimum size available is still smaller than the one needed. The calculated and measured circumference values indicate that the head probe's design can accommodate normal head shape variations and the whole range of male and female head sizes.[50,51] Also, the preauricular arc length range (144 to 407 mm) that the head probe provides is larger than the values measured on human heads (374.7 ± 25.29 mm).[53] The measured value for the maximum inion-to-nasion arc is lower than its calculated value because the smaller arcs in the back-to-front direction currently prevent it from expanding to its maximum extent. We have modified the

Table 1 Maximum and minimum arc dimensions for head circumference (C), inion-to-nasion arc (IN) and preauricular arc (P).

Segment	Calculated length (mm)	Measured length (mm)
$x_{\max,d_1}$	20.4	—
$x_{\max,d_2}$	17.2	—
$x_{\min,d_1}$	7.2	—
$x_{\min,d_2}$	7.4	—
$C_{\max_{(d_2)}}$	689	650
$C_{\min_{(d_2)}}$	297	400
$\mathrm{IN}_{\min_{(d_1)}}$	407	378
$\mathrm{IN}_{\min_{(d_1)}}$	144	270
$P_{\max_{(d_1)}}$	407	405
$P_{\min_{(d_1)}}$	144	305

dimensions of those arcs for future prototypes in order to achieve the maximum expansion possible of the probe. The inion-to-nasion arc length range (144 to 407 mm) from the head probe is larger than the reported values for the arc from the glabella to the inion, also referred to as the external occipital protuberance, (329 ± 12 mm) for males between the ages of 18 and 25.[54] It must be noted that there is a small distance from the glabella (situated between the eyebrows) and the nasion. However, the arc lengths can still be used for comparison given that the maximum inion-to-nasion arc length value from the head probe is significantly larger than the maximum glabella-to-nasion arc length value reported.

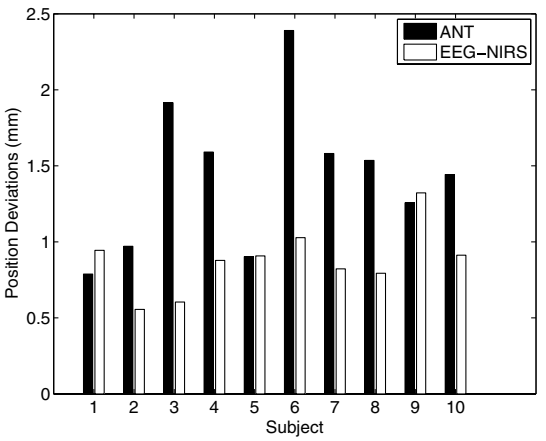

Fig. 8 Standard deviation from mean position for 10 subjects (mm) averaged across three runs for ANT Waveguard probe (black) and NIRS-EEG probe (white).

Table 2 Analysis of variance: constrained (Type III) sums of squares. Statistical analysis of the positional errors accounting for variation across subjects, electrode locations, and probe.

Source	Sum Sq.	d.f.	Mean Sq.	*F*	Prob > *F*
Subject	144.3	9	16.0	30.5	<0.001
Locations	470.0	64	7.3	14.0	<0.001
Probe	162.6	1	162.6	309.0	<0.001
Error	1473.0	2800	0.5		
Total	2314.0	2874			

3.2 *Sensor Positioning Precision and Accuracy Test*

The errors for the positional precision test were calculated individually for each subject before performing a global analysis. As shown in Fig. 8, the mean error computed for each subject is smaller for the NIRS-EEG probe in seven out of the ten subjects. On average over the 10 subjects, the NIRS-EEG probe has significantly smaller mean positional precision error.

Multifactor ANOVA statistics were computed from the errors for each run to account for subject, electrode locations, and probe variation, as seen in Table 2. The mean positional errors are plotted in Fig. 9, which shows the standard deviation from mean position for all probe locations. This was calculated to analyze the repeatability of the positions, or whether the positions will be placed in the same location every time the probe is affixed to the same subject.

Figure 9 shows the precision of the NIRS-EEG probe compared to the ANT probe; it shows how precisely the sensors are placed on the same location on a particular head every time they are affixed. Statistical results from ANOVA show that the NIRS-EEG probe (0.89 ± 0.23 mm) is more precise than the ANT probe (1.47 ± 0.36 mm). The electrodes are placed in the corresponding location with a mean precision of 0.89 mm when the probe is affixed several times. The precision is observed at different levels for each subject on the results shown in Fig. 8.

For the positional accuracy test, errors were calculated as

$$\epsilon = \sqrt{\left[\frac{1}{\mathrm{NM}}\left(\sum_{n=1}^{N}\sum_{m=1}^{M}\frac{s}{l}100\% - p\right)\right]^2}, \qquad (7)$$

for $N = 10$ subjects and $M = 3$ runs, where s is the segment length between two electrodes in an arc, l is the total length of the arc computed as the sum of all segments, and p is either 10% or 20%, for either the 10–10 system or the 10–20

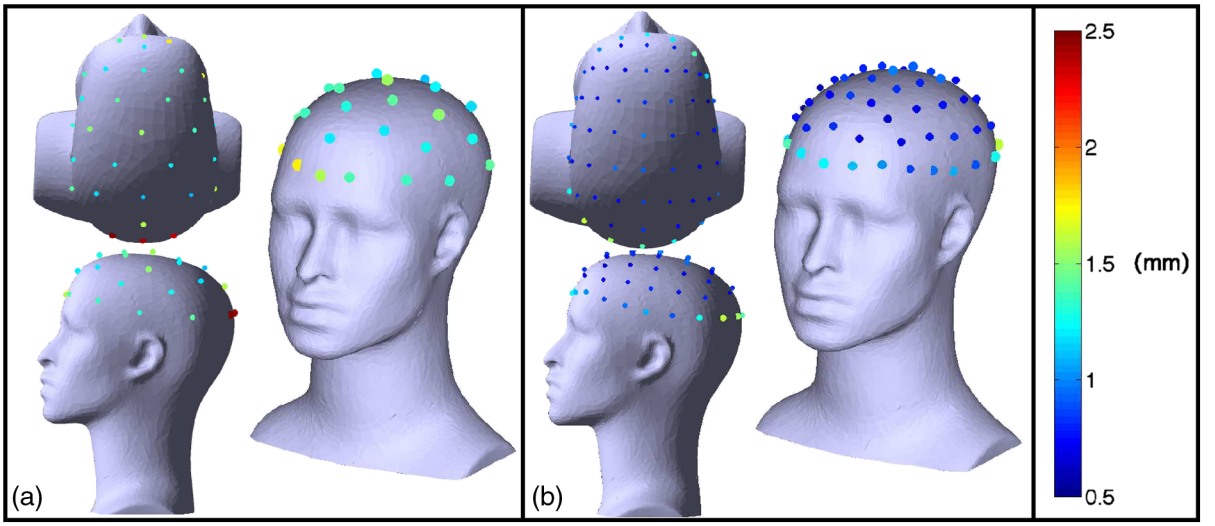

Fig. 9 Standard deviation in scalp positions for ANT Waveguard probe (1.47 ± 0.36 mm) (a) and NIRS-EEG probe (0.89 ± 0.23 mm) (b).

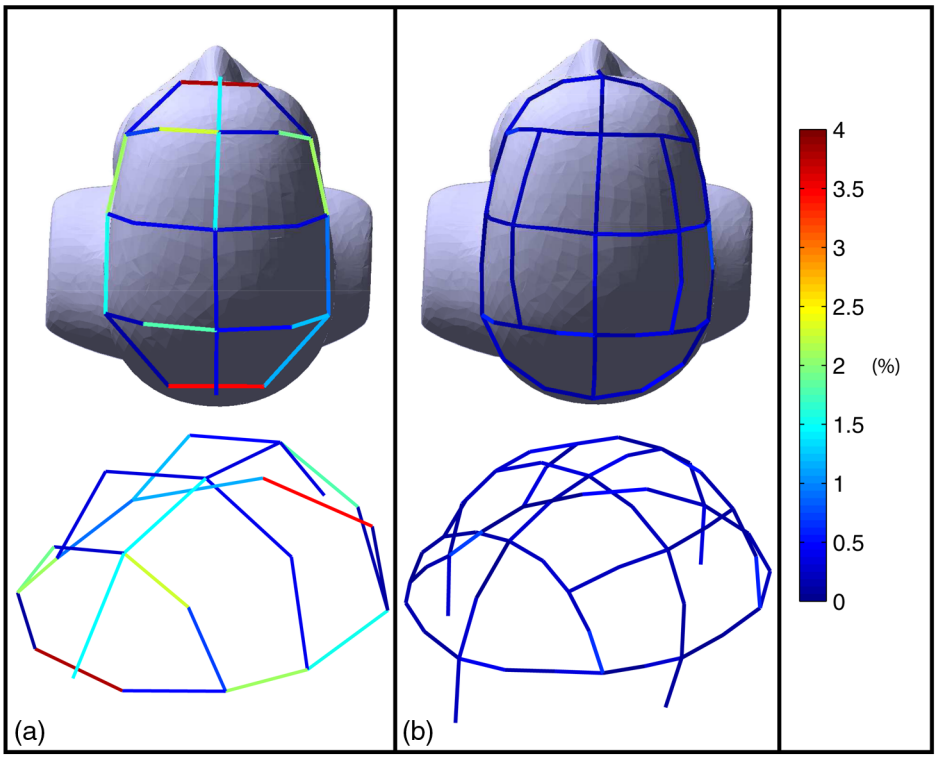

Fig. 10 Root-mean-squared error in the percent of total arc length for segments of the ANT Waveguard probe ($1.13 \pm 1.02\%$) (a) and NIRS-EEG probe ($0.19 \pm 0.15\%$) (b).

international system. Figure 10 shows the percent error of the distance between positions for both probes. This was calculated to analyze the accuracy of the positions relative to the standard 10–10 and 10–20 system.

Figure 10 shows the arc length accuracy of the ANT and NIRS-EEG probes relative to the 10–10 system. Error calculations show that the NIRS-EEG probe ($0.19 \pm 0.15\%$) has improved accuracy over the ANT probe ($1.13 \pm 1.02\%$). This means that when the probe is placed on the subject, the electrodes are much closer to where they should be according to the standard 10–10 arrangement in the NIRS-EEG probe.

3.3 *Web Volumetric Isotensile Test*

Figure 11 shows histograms of the forces measured at displacements of 0.5, 0.75, and 1 cm. The three distinct peaks on both graphs that appear for each distance shows the uniformity in the forces across the surface of the head. The smaller peaks on the left plot correspond to the forces in the headband positions which appear to be lower than those on the right plot, which show forces on the rest of the web. This can also be observed in Fig. 12.

A linear regression was performed on the three measurements per node to calculate the slope and intercept of the linear fit to the data. Figure 12 shows the force exerted by the members at each node by pulling the node 5 mm away from the head as determined by the linear regression.

4 Discussion

The design details and mechanical properties of a head probe are important determinants of NIRS and EEG data quality. We have presented the design and evaluated a proposed novel probe. The main arc-lengths obtained show that the NIRS-EEG head probe mechanism can mechanically adjust to a wide range of head

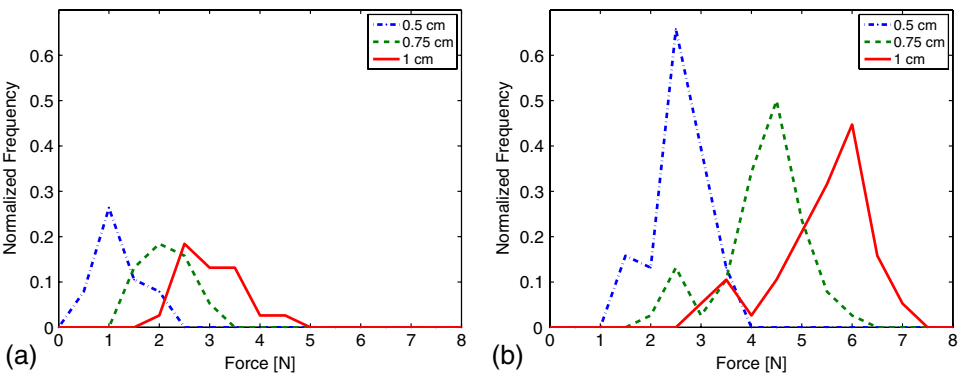

Fig. 11 Histogram of forces at 0.5, 0.75, and 1 cm normal to the head divided into nodes on the headband (a) and the rest of nodes (b).

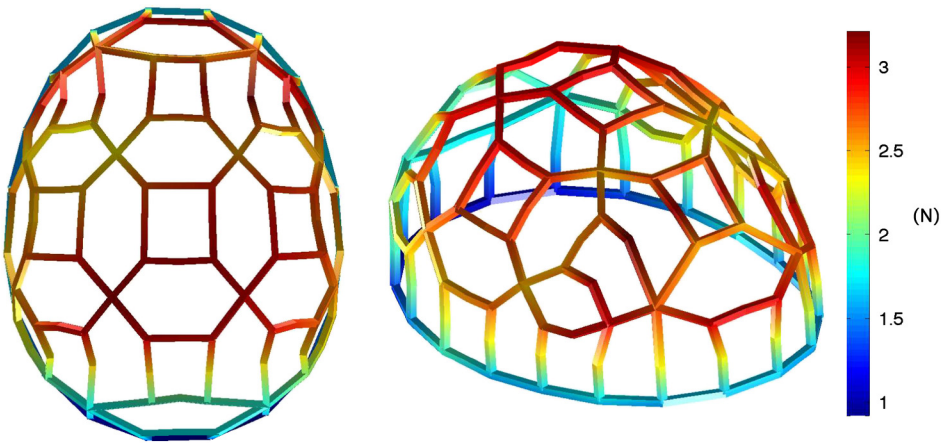

Fig. 12 Force at 5 mm away from head $\bar{F} = 2.28 \pm 0.88$ N (The web model used is for visualization purposes only and has members with equal cross-sectional area).

sizes. The NIRS-EEG head probe also shows an improvement of 39.5% in precision and 83.2% in accuracy over the commercial product that we tested. The results from our proposed NIRS-EEG probe also compare favorably to the precision error reported in studies evaluating a NeuroMedical cap (Compumedics USA, El Paso, Texas), which ranged from 3.0 to 12.7 mm.[39] Studies of the projection of the 10–10 positions onto the brain show a standard deviation of 4.6 mm in x, 7.1 mm in y and 7.8 mm in z,[55] which is larger than the error introduced by our NIRS-EEG head probe.

The uniform contact force of the proposed NIRS-EEG head probe is expected to provide a more consistent contact pressure from optodes and help maintain consistent optical coupling. The uniformity in the optode pressure could also enhance subject comfort.

There is still room for improvement in the proposed NIRS-EEG probe design. A few positions in the lower headband appear to have lower pressure to the head than the average node, which will be taken into account when designing the next version. These lower forces could be caused by the lack of web members pulling down towards the neck at those positions, which eliminates the feasibility of attaining equilibrium at the node.

Future work will focus on evaluating optode and electrode designs and coupling to the scalp, determining of EEG and NIRS data quality using the head probe, and assessing the stability of the probe during head movements by quantifying motion artifacts. The probe is manufactured without ferromagnetic materials for compatibility with MRI and magnetoencephalography (MEG) and is designed with low profile to fit inside MRI head coils or MEG dewars. Studies exploring the compatibility of the NIRS-EEG probe with these systems will also be carried out.

5 Conclusion

The NIRS-EEG head probe is a versatile solution to the problem of placing sensors on the head for simultaneous noninvasive neural and hemodynamic brain monitoring. Tests to determine structural and mechanical properties of the probe demonstrated the accuracy, precision, and force uniformity in the sensor placement. The design of the NIRS-EEG probe accommodates a wide range of head size and shape variability and standard clinical electrode placement, which could facilitate use of NIRS and EEG in the clinical setting.

Acknowledgments

This work was supported by the United States Department of Education P116Z080112, the NIH National Institute of Aging R21AG033256, and Rogue Research Inc. The NIRS-EEG head probe described in this work is patent-pending and has been licensed to Rogue Research Inc.

References

1. M. A. Franceschini et al., "Coupling between somatosensory evoked potentials and hemodynamic response in the rat," *NeuroImage* **41**(2), 189–203 (2008).
2. C. I. Moore and R. Cao, "The hemo-neural hypothesis: on the role of blood flow in information processing," *J. Neurophysiol.* **99**(5), 2035–2047 (2008).
3. L. Rovati et al., "Optical and electrical recording of neural activity evoked by graded contrast visual stimulus," *Biomed. Eng. OnLine* **6**(28), 1–15 (2007).
4. F. Wallois et al., "EEG-NIRS in epilepsy in children and neonates," *Clin. Neurophysiol.* **40**(5–6), 281–292 (2010).
5. J. Furusho et al., "Simultaneous study of interictal EEG and near-infrared spectroscopy in a boy with epilepsy," *Int. Congress Ser.* **1232**, 673–676 (2002).
6. N. Roche-Labarbe et al., "NIRS-measured oxy- and deoxyhemoglobin changes associated with EEG spike-and-wave discharges in children," *Epilepsia* **49**(11), 1871–1880 (2008).
7. Y. Shang et al., "Cerebral monitoring during carotid endarterectomy using near-infrared diffuse optical spectroscopies and electroencephalogram," *Phys. Med. Biol.* **56**(10), 3015–3032 (2011).
8. T. Näsi et al., "Combining near-infrared spectroscopy with electroencephalography and repetitive transcranial magnetic stimulation," *Proc. SPIE* **7369**, 736905 (2009).
9. H. Laufs, "A personalized history of EEG-fMRI integration," *NeuroImage* **62**(2), 1056–1067 (2012).
10. B.-M. Mackert et al., "Neurovascular coupling analyzed non-invasively in the human brain," *NeuroReport* **15**(1), 63–66 (2004).
11. B. He et al., "Electrophysiological imaging of brain activity and connectivity-challenges and opportunities," *IEEE Trans. Biomed. Eng.* **58**(7), 1918–1931 (2011).
12. R. L. Savoy, "History and future directions of human brain mapping and functional neuroimaging," *Acta Psychol.* **107**(1–3), 9–42 (2001).
13. A. Machado et al., "Detection of hemodynamic responses to epileptic activity using simultaneous electro-encephalography (EEG)/near infra

red spectroscopy (NIRS) acquisitions," *NeuroImage* **56**(1), 114–125 (2011).
14. O. J. Arthurs et al., "Intracortically distributed neurovascular coupling relationships within and between human somatosensory cortices," *Cerebral Cortex* **17**(3), 661–668 (2007).
15. W. Ou et al., "Study of neurovascular coupling in humans via simultaneous magnetoencephalography and diffuse optical imaging acquisition," *NeuroImage* **46**(3), 624–632 (2009).
16. C. Iadecola, "Neurovascular regulation in the normal brain and in Alzheimer's disease," *Nature Rev.* **5**(5), 347–360 (2004).
17. B. V. Zlokovic, "The blood-brain barrier in health and chronic neurodegenerative disorders," *Neuron* **57**(2), 178–201 (2008).
18. C. Iadecola, "The overlap between neurodegenerative and vascular factors in the pathogenesis of dementia," *Acta Neuropathol.* **120**(3), 287–296 (2010).
19. H. Girouard and C. Iadecola, "Neurovascular coupling in the normal brain and in hypertension, stroke, and Alzheimer disease," *J. Appl. Physiol.* **100**(1), 328–335 (2006).
20. S. Guo and E. H. Lo, "Dysfunctional cell-cell signaling in the neurovascular unit as a paradigm for central nervous system disease," *Stroke* **40**(Suppl 1), S4–S7 (2009).
21. B. Rosengarten et al., "Neurovascular coupling in Alzheimer patients: effect of acetylcholine-esterase inhibitors," *Neurobiol. Aging* **30**(12), 1918–1923 (2009).
22. J. A. Claassen and R. Zhang, "Cerebral autoregulation in Alzheimer's disease," *J. Cereb. Blood Flow Metab.* **31**(7), 1572–1577 (2011).
23. H. Radhakrishnan et al., "Study of neurovascular coupling by modulating neuronal activity with GABA," *Brain Res.* **1372**, 1–12 (2011).
24. P. L. Nunez and R. Srinivasan, *Electric Fields of the Brain: The Neurophysics of EEG*, 2nd ed., Oxford University Press, New York (2006).
25. A. Gallagher et al., "Non-invasive pre-surgical investigation of a 10 year-old epileptic boy using simultaneous EEG-NIRS," *Seizure* **17**(6), 576–582 (2008).
26. S. Lloyd-Fox, A. Blasi, and C. E. Elwell. "Illuminating the developing brain: the past, present and future of functional near infrared spectroscopy," *Neurosci. Biobehav. Rev.* **34**(3), 269–284 (2010).
27. K. L. Perdue, Q. Fang, and S. G. Diamond, "Quantitative assessment of diffuse optical tomography sensitivity to the cerebral cortex using a whole-head probe," *Phys. Med. Biol.* **57**(10), 2857–2872 (2012).
28. Y. Hoshi, "Functional near-infrared spectroscopy: potential and limitations in neuroimaging studies," *Int. Rev. Neurobiol.* **66**, 237–266 (2005).
29. S. R. Arridge, M. Cope, and D. T. Delpy, "The theoretical basis for the determination of optical pathlengths in tissue: temporal and frequency analysis," *Phys. Med. Biol.* **37**(7), 1531–1560 (1992).
30. A. Villringer and U. Dirnagl, "Coupling of brain activity and cerebral blood flow: basis of functional neuroimaging," *Cerebrovasc. Brain Metab. Rev.* **7**(3), 240–276 (1995).
31. R. E. Gagnon and A. J. Macnab, "Near infrared spectroscopy (NIRS) in the clinical setting An adjunct to monitoring during diagnosis and treatment," *Spectroscopy* **19**(5–6), 221–233 (2005).
32. A. Villringer et al., "Near infrared spectroscopy (NIRS): a new tool to study hemodynamic changes during activation of brain function in human adults," *Neurosci. Lett.* **154**(1–2), 101–104 (1993).
33. G. H. Klem et al., "The ten-twenty electrode system of the International Federation. Recommendations for the practice of clinical neurophysiology: guidelines of the International Federation of clinical physiology," *Electroencephalogr. Clin. Neurophysiol.* **52**, 3–6 (1999).
34. T. Gasser, P. Bächer, and H. Steinberg. "Test-retest reliability of spectral parameters of the EEG," *Electroencephalogr. Clin. Neurophysiol* **60**(4), 312–319 (1985).
35. V. L. Towle et al., "The spatial location of EEG electrodes: locating the best-fitting sphere relative to cortical anatomy," *Electroencephalogr. Clin. Neurophysiol.* **86**(1), 1–6 (1993).
36. M. Okamoto et al., "Three-dimensional probabilistic anatomical cranio-cerebral correlation via the international 1020 system oriented for transcranial functional brain mapping," *NeuroImage* **21**(1), 99–111 (2004).
37. M. A. Franceschini et al., "Diffuse optical imaging of the whole head," *J. Biomed. Opt.* **11**(5), 054007 (2006).
38. M. Takeuchi et al., "Brain cortical mapping by simultaneous recording of functional near infrared spectroscopy and electroencephalograms from the whole brain during right median nerve stimulation," *Brain Topogr.* **22**(3), 197–214 (2009).
39. S. R. Atcherson et al., "Variability of electrode positions using electrode caps," *Brain Topogr.* **20**(2), 105–111 (2007).
40. J. E. Hall and A. C. Guyton, *Guyton and Hall Textbook of Medical Physiology*, 12th ed., Saunders/Elsevier, Philadelphia (2011).
41. E. S. Kappenman and S. J. Luck, "The effects of electrode impedance on data quality and statistical significance in ERP recordings," *Psychophysiology* **47**(5), 888–904 (2010).
42. T. C. Ferree et al., "Scalp electrode impedance, infection risk, and EEG data quality," *Clin. Neurophysiol.* **112**(3), 536–544 (2001).
43. M. S. Fernandes et al., "Hydrogel-based photonic sensor for a biopotential wearable recording system," *Biosens. Bioelectron.* **26**(1), 80–86 (2010).
44. V. V. Nikulin, J. Kegeles, and G. Curio, "Miniaturized electroencephalographic scalp electrode for optimal wearing comfort," *Clin. Neurophysiol.* **121**(7), 1007–1014 (2010).
45. A. Searle and L. Kirkup, "A direct comparison of wet, dry and insulating bioelectric recording electrodes," *Physiol. Meas.* **21**(2), 271–283 (2000).
46. T. E. J. Noponen et al., "Effects of improper source coupling in frequency-domain near-infrared spectroscopy," *Phys. Med. Biol.* **55**(10), 2941–60 (2010).
47. T. Yamada, S. Umeyama, and K. Matsuda, "A multidistance probe arrangement NIRS for detecting absorption changes in cerebral gray matter layer," *Proc. SPIE* **7557**, 75570X (2010).
48. V. Jurcak, D. Tsuzuki, and I. Dan, "10/20, 10/10, and 10/5 systems revisited: their validity as relative head-surface-based positioning systems," *NeuroImage* **34**(4), 1600–1611 (2007).
49. R. Oostenveld and P. Praamstra, "The five percent electrode system for high-resolution EEG and ERP measurements," *Clin. Neurophysiol.* **112**(4), 713–719 (2001).
50. K. M. D. Bushby et al., "Centiles for adult head circumference," *Arch. Dis. Child.* **67**(10), 1286–1287 (1992).
51. J. D. Rollins, J. S. Collins, and K. R. Holden, "United States head circumference growth reference charts: birth to 21 years," *J. Pediatr.* **156**(6), 907–913 (2010).
52. R. Vincent, "BrainWeb: simulated brain database," http://www.bic.mni.mcgill.ca/brainweb/ (19 October 2012).
53. H. Saberi et al., "Correlation of cephalic anthropometric parameters and microsurgical anatomy of the optic nerves: a cadaveric morphometric study." *Surg. Neurol.* **60**(5), 438–442 (2003).
54. E. A. Christofides and M. E. Steinmann, "A novel anthropometric chart for craniofacial surgery," *J. Craniofacial Surg.* **21**(2), 352–357 (2010).
55. L. Koessler et al., "Automated cortical projection of EEG sensors: anatomical correlation via the international 10–10 system," *NeuroImage* **46**(1), 64–72 (2009).